npj | Quantum Materials

www.nature.com/npjquantmats

ARTICLE OPEN

Check for updates

Tunable 3D/2D magnetism in the $(MnBi_2Te_4)(Bi_2Te_3)_m$ topological insulators family

Ilya I. Klimovskikh[1]✉, Mikhail M. Otrokov[2,3]✉, Dmitry Estyunin[1], Sergey V. Eremeev[1,4,5], Sergey O. Filnov[1], Alexandra Koroleva[1], Eugene Shevchenko[1], Vladimir Voroshnin[6], Artem G. Rybkin[1], Igor P. Rusinov[1,5], Maria Blanco-Rey[7,8], Martin Hoffmann[9], Ziya S. Aliev[10,11], Mahammad B. Babanly[12,13], Imamaddin R. Amiraslanov[11,13], Nadir A. Abdullayev[11,13], Vladimir N. Zverev[14], Akio Kimura[15], Oleg E. Tereshchenko[1,16,17], Konstantin A. Kokh[1,17,18], Luca Petaccia[19], Giovanni Di Santo[19], Arthur Ernst[9,20], Pedro M. Echenique[2,7,8], Nazim T. Mamedov[11], Alexander M. Shikin[1] and Eugene V. Chulkov[1,2,7,8]✉

Feasibility of many emergent phenomena that intrinsic magnetic topological insulators (TIs) may host depends crucially on our ability to engineer and efficiently tune their electronic and magnetic structures. Here we report on a large family of intrinsic magnetic TIs in the homologous series of the van der Waals compounds $(MnBi_2Te_4)(Bi_2Te_3)_m$ with $m = 0, \cdots, 6$. Magnetic, electronic and, consequently, topological properties of these materials depend strongly on the m value and are thus highly tunable. The antiferromagnetic (AFM) coupling between the neighboring Mn layers strongly weakens on moving from $MnBi_2Te_4$ ($m = 0$) to $MnBi_4Te_7$ ($m = 1$) and $MnBi_6Te_{10}$ ($m = 2$). Further increase in m leads to change of the overall magnetic behavior to ferromagnetic (FM) one for ($m = 3$), while the interlayer coupling almost disappears. In this way, the AFM and FM TI states are, respectively, realized in the $m = 0$, 1, 2 and $m = 3$ cases. For large m numbers a hitherto-unknown topologically nontrivial phase can be created, in which below the corresponding critical temperature the magnetizations of the non-interacting 2D ferromagnets, formed by the $MnBi_2Te_4$ building blocks, are disordered along the third direction. The variety of intrinsic magnetic TI phases in $(MnBi_2Te_4)(Bi_2Te_3)_m$ allows efficient engineering of functional van der Waals heterostructures for topological quantum computation, as well as antiferromagnetic and 2D spintronics.

npj Quantum Materials (2020)5:54 ; https://doi.org/10.1038/s41535-020-00255-9

INTRODUCTION

Magnetism and topology can meet each other both in real space, giving rise to complex magnetic structures such as vortices or skyrmions, and in reciprocal momentum space, resulting in Weyl semimetal or magnetic topological insulator (MTI) phases. In the MTI case, the interplay between topology and magnetism provides particularly rich playground for realization of exotic physics. Below the magnetic critical temperature, the time-reversal symmetry breaks down introducing a mass term to the linear dispersion of Dirac fermions thus opening opportunities for realization of such phenomena as quantized anomalous Hall (QAH) and magnetoelectric effect, axion electrodynamics, or Majorana fermions[1–5]. These unusual properties make MTIs extremely attractive for applications in novel electronics and in the emerging 2D[6–8] and antiferromagnetic (AFM) spintronics[9–11].

Until recently, the magnetism in topological insulators (TIs) has been achieved using either magnetic doping[3,4,12–16], or proximity effect[17,18] as well as by construction of van der Waals (vdW) heterostructures[19–23]. This situation has changed drastically with the recent discovery of the AFM TI phase[24] in stoichiometric vdW-layered antiferromagnet $MnBi_2Te_4$[25–29], which inspired a lot of research activity as it holds promise for realization of the high-temperature QAH and axion insulator states, Majorana hinge modes and other effects[24,26–28,30–34].

Here we propose the MTI family by introducing the $(MnBi_2Te_4)(Bi_2Te_3)_m$ series of vdW materials that, apart from $MnBi_2Te_4$ ($m = 0$), contains six more topologically nontrivial compounds, namely $MnBi_4Te_7$ ($m = 1$), $MnBi_6Te_{10}$ ($m = 2$), $MnBi_8Te_{13}$ ($m = 3$), $MnBi_{10}Te_{16}$ ($m = 4$), $MnBi_{12}Te_{19}$ ($m = 5$), and $MnBi_{14}Te_{22}$ ($m = 6$). Along the series, the strength of the interlayer exchange interaction, that couples neighboring FM Mn layers, gradually decreases with the increase of m, while the overall magnetic ordering changes from an AFM ($m = 0$, 1, 2) to FM ($m = 3$). Combined with the non-trivial topology of the $(MnBi_2Te_4)(Bi_2Te_3)_m$ compounds, these magnetic states give rise to the AFM and FM TI phases for $m = 0$, 1, 2 and $m = 3$, respectively. For large m numbers a new MTI phase can be formed in which, below the respective T_C, the magnetizations of the 2D FM-ordered Mn layers of the $MnBi_2Te_4$ building blocks are disordered along the [0001]

[1]Saint Petersburg State University, 198504 Saint Petersburg, Russia. [2]Centro de Física de Materiales (CFM-MPC), Centro Mixto CSIC-UPV/EHU, 20018 Donostia-San Sebastián, Basque Country, Spain. [3]IKERBASQUE, Basque Foundation for Science, 48011 Bilbao, Spain. [4]Institute of Strength Physics and Materials Science, Russian Academy of Sciences, 634055 Tomsk, Russia. [5]Tomsk State University, 634050 Tomsk, Russia. [6]Helmholtz-Zentrum Berlin für Materialien und Energie, Elektronenspeicherring BESSY II, Albert-Einstein-Straße 15, 12489 Berlin, Germany. [7]Departamento de Física de Materiales UPV/EHU, 20080 Donostia-San Sebastián, Basque Country, Spain. [8]Donostia International Physics Center (DIPC), 20018 Donostia-San Sebastián, Basque Country, Spain. [9]Institut für Theoretische Physik, Johannes Kepler Universität, A 4040 Linz Austria. [10]Azerbaijan State Oil and Industry University, AZ1010 Baku, Azerbaijan. [11]Institute of Physics, National Academy of Sciences of Azerbaijan, AZ1143 Baku, Azerbaijan. [12]Institute of Catalysis and Inorganic Chemistry, Azerbaijan National Academy of Science, AZ1143 Baku, Azerbaijan. [13]Baku State University, AZ1148 Baku, Azerbaijan. [14]Institute of Solid State Physics RAS, Chernogolovka, Moscow district, Russia. [15]Department of Physical Sciences, Graduate School of Science, Hiroshima University, 1-3-1 Kagamiyama, Higashi-Hiroshima 739-8526, Japan. [16]A.V. Rzhanov Institute of Semiconductor Physics, Novosibirsk 630090, Russia. [17]Novosibirsk State University, Novosibirsk 630090, Russia. [18]V.S. Sobolev Institute of Geology and Mineralogy, Siberian Branch, Russian Academy of Sciences, Novosibirsk 630090, Russian Federation. [19]Elettra Sincrotrone Trieste, Strada Statale 14 km 163.5, 34149 Trieste, Italy. [20]Max-Planck-Institut für Mikrostrukturphysik, Weinberg 2, D-06120 Halle, Germany. ✉email: ilya.klimovskikh@spbu.ru; mikhail.otrokov@gmail.com; evguenivladimirovich.tchoulkov@ehu.es

direction. The topologically nontrivial nature of these compounds is confirmed by angle-resolved photoemission spectroscopy (ARPES) measurements that reveal the presence of the topological surface states (TSS) whose dispersion depends strongly on the crystal surface termination. The unusual magnetic properties make the $(MnBi_2Te_4)(Bi_2Te_3)_m$ series a unique tunable platform for creating various exotic states of matter, such as intrinsic axion or QAH insulator[20,26,32], the field-induced QH phase[31,32], high-order Möbius insulator[35], or chiral topological superconductor[33].

RESULTS AND DISCUSSION

CRYSTAL STRUCTURE AND MAGNETIC CROSSOVER

The first compound in the $(MnBi_2Te_4)(Bi_2Te_3)_m$ series is $MnBi_2Te_4$ ($m = 0$), which had been investigated previously and discovered to be the first AFM TI[25,36]. This system consists of septuple layer (SL) blocks stacked one on top of another. Each SL is a 2D ferromagnet, while the coupling between the neighboring SLs is AFM[25,37]. For $m \geq 1$, the members of the $(MnBi_2Te_4)(Bi_2Te_3)_m$ family are comprised of alternating septuple ($MnBi_2Te_4$) and quintuple (Bi_2Te_3) layer blocks (see Fig. 1a). The growth details and crystal structures of thus-formed $MnBi_4Te_7$ and $MnBi_6Te_{10}$ compounds have been first reported in ref. [38], for which the -5-7-5-7- and -5-5-7-5-5-7- blocks sequences corresponding to $m = 1$ and $m = 2$ have been revealed, respectively.

The XRD patterns of our $MnBi_4Te_7$, $MnBi_6Te_{10}$, $MnBi_8Te_{13}$, $MnBi_{10}Te_{16}$, $MnBi_{12}Te_{19}$, and $MnBi_{14}Te_{22}$ samples, shown in Supplementary Fig. 1, confirm their $P\bar{3}m1$ and $R\bar{3}m$ space groups.

The temperature dependence of the resistivity measured in a zero magnetic field demonstrates the metallic-like behavior for both $MnBi_4Te_7$ and $MnBi_6Te_{10}$ (see Fig. 1b, c). At low temperatures, the well-defined kinks at 13.2 K ($MnBi_4Te_7$) and 11.9 K ($MnBi_6Te_{10}$) are observed for both compounds. As the external magnetic field is switched on and increased these features are washed out, pointing towards their magnetic origin.

The field-cooled (FC) and zero-field cooled (ZFC) magnetic susceptibilities measured at 0.1 T for $MnBi_4Te_7$ are shown in Fig. 1d (blue curve). The high temperature paramagnetic behavior ends up with a pronounced peak at 13 K, that is characteristic of an AFM ordering. The fitting of the susceptibility by the Curie–Weiss law yields the Curie–Weiss temperature (Θ_{CW}) of 13.2 K. Positive sign and relatively high value of Θ_{CW} (cf. 3–6 K for $MnBi_2Te_4$[25]) indicate the presence of strong ferromagnetic interactions in $MnBi_4Te_7$ in spite of the overall AFM behavior. The Néel temperature of only 13 K for $MnBi_4Te_7$ versus 25 K for $MnBi_2Te_4$ reveals a strong weakening of the interlayer AFM coupling due to the insertion of the non-magnetic quintuple layer block (QL) between neighboring SLs. The onset of the

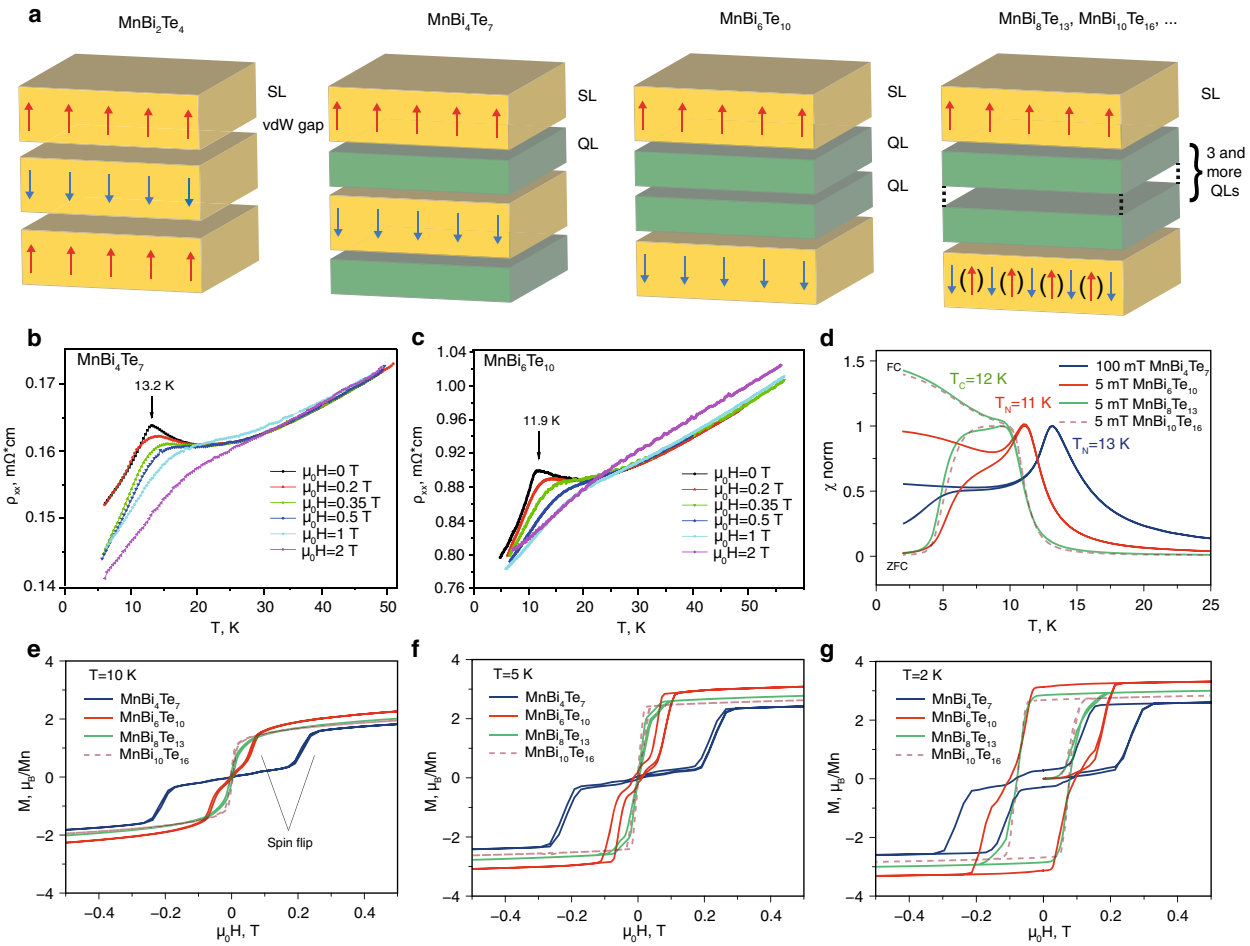

Fig. 1 **a** Compounds $(MnBi_2Te_4)(Bi_2Te_3)m$ consist of alternating five-layer (QL) and magnetic seven-layer (SL) blocks. **b**, **c** Temperature dependence of the resistivity for $MnBi_4Te_7$ and $MnBi_6Te_{10}$ for various applied out-of-plane magnetic fields. **d** Normalized magnetic susceptibility for $MnBi_4Te_7$, $MnBi_6Te_{10}$, $MnBi_8Te_{13}$, and $MnBi_{10}Te_{16}$ as a function of temperature measured in a small magnetic field in zero-field-cooled and field-cooled conditions. **d**, **e** Field-dependent magnetization curves taken at various temperatures with out-of-plane external magnetic field for $MnBi_4Te_7$, $MnBi_6Te_{10}$, $MnBi_8Te_{13}$, and $MnBi_{10}Te_{16}$.

ferromagnetic interactions is also manifested in splitting of the FC and ZFC curves at low temperature (spin-glass-like transition).

Increasing by one the number of QLs between SLs and forming $MnBi_6Te_{10}$ leads to further weakening of the interlayer exchange interaction. The magnetic susceptibility data for this compound, shown in Fig. 1d (red curve), exhibit similar cusp at low temperature, signaling the AFM ordering, but the Néel temperature decreases to 11 K in this case. Furthermore, below 10 K FC and ZFC curves splitting becomes larger than for $MnBi_4Te_7$, thus showing the enhanced competition between AFM and FM couplings.

The $m = 3$ and 4 members of the series, i.e. $MnBi_8Te_{13}$ and $MnBi_{10}Te_{16}$, show an overall ferromagnetic behavior below the Curie temperatures of about 12 K, as revealed by the magnetization measurements (Fig. 1d); a similar behavior is expected for $MnBi_{12}Te_{19}$ ($m = 5$) and $MnBi_{14}Te_{22}$ ($m = 6$) because of the vanishing interlayer exchange interaction.

The $M(H)$ curves for $m = 1$–4 compounds taken at various temperatures are presented in Fig. 1e–g. Slightly below the Néel temperature (10 K) for $MnBi_4Te_7$ a typical AFM $M(H)$ behavior takes place, with a spin–flip upturns appearing at 0.2 T, the latter value being much lower than that for $MnBi_2Te_4$ (3.5 T)[25]. The gradual reduction of interlayer exchange interaction leads to further decrease of this value, the $M(H)$ dependence for $MnBi_6Te_{10}$ compound (red curve in Fig. 1e) exhibits the spin–flip transition at about ~0.07 T. The next members of the MBT family, i.e. $MnBi_8Te_{13}$ and $MnBi_{10}Te_{16}$ demonstrate rather conventional ferromagnetic s-like curves.

At very low temperatures ($T = 5$ and 2 K), the spin–flip hysteresis opens up in the magnetic field interval from 0.1 to 0.3 T for $m = 1$ system, as seen in Fig. 1f, g. The $m = 2$ compound exhibits the same behavior, but at lower external fields. Moreover, at 2 K, in the absence of external field, the magnetization does not fall to zero and forms a ferromagnetic hysteresis loop with small and large remanence for $m = 1$ and 2, respectively. Such a dual complex metamagnetic behavior can be explained by the presence of domains with ferromagnetic and AFM ordering between neighbor SLs. However, in case of $m = 2$ the remanence close to saturation shows that forced FM state can survive at zero and even at small negative magnetic fields when the thermal fluctuations are weak enough. Similar results with the metamagnetic behavior of $MnBi_4Te_7$ and $MnBi_6Te_{10}$ have been reported recently in refs. [39–43]. The $m = 3$ ($MnBi_8Te_{13}$) compound clearly demonstrates an almost pure ferromagnetic hysteresis loops, only some small deviations from s-like curve can be distinguished at $T = 5$ K. Note, that 3D FM ordering for $MnBi_8Te_{13}$ has been claimed in ref. [44]. The presented data testify the weakening of 3D AFM coupling with m number increase and strong 2D FM intralayer coupling for all compounds.

The described experimental picture is consistent with that yielded by theory. Namely, the DFT exchange coupling parameters calculations reveal, first, a stable tendency to the intralayer FM ordering in the SLs of $MnBi_4Te_7$ and, second, a strong drop of the interlayer exchange coupling (1–2 orders of magnitude) as compared to $MnBi_2Te_4$ (see Supplementary Note 3). Highly accurate total-energy calculations give an energy difference between the FM and interlayer AFM configurations of 0.25 meV per Mn pair in favor of the interlayer AFM one. The magnetic anisotropy energy, E_a, is positive and equals to 0.12 meV (i.e. the easy axis is out-of-plane), which is roughly two times smaller than in bulk $MnBi_2Te_4$. In good agreement with the resistivity and magnetization measurements, our Monte Carlo simulations yield a Néel temperature of 13.6 K for the bulk $MnBi_4Te_7$. The drop of the Néel temperature from about 25 K in $MnBi_2Te_4$ to $\simeq$13 K in $MnBi_4Te_7$ is precisely caused by the weakening of the interlayer exchange coupling.

The DFT total-energy calculations performed for $MnBi_6Te_{10}$ show that the interlayer coupling weakens with respect to the $MnBi_4Te_7$ case, the difference between the AFM and FM states being 0.1 meV in favor of the AFM ordering. These results are highly consistent with the experiment, where an AFM ground state has been found for $MnBi_6Te_{10}$, while a small external field of ~0.1 T is enough to force the FM ordering, that can survive at zero and some negative magnetic fields at low temperature.

In ref. [26], the Curie temperature of the free-standing $MnBi_2Te_4$ SL has theoretically been predicted to be 12 K, which coincides with the corresponding values for $MnBi_8Te_{13}$ and $MnBi_{10}Te_{16}$ (see Fig. 1d). These facts allow us to conclude that the interlayer exchange coupling between SLs vanishes in $(MnBi_2Te_4)(Bi_2Te_3)_m$ family for $m > 3$ and in the case of absence of the free carriers their magnetic structure can be described as a set of decoupled 2D ferromagnets whose magnetizations are randomly oriented—either parallel or antiparallel to the [0001] direction. Owing to the n-doping of the samples, the long-range RKKY exchange interaction may still weakly couple the magnetic layer blocks even for $m > 3$, although no indication of that has been observed in the experiment. Notably, some small concentration of Bi/Mn defects (~3%, see Supplementary Note 2 and ref. [45]) can slightly influence magnetic properties, that requires further investigations. Thus, the interlayer exchange interaction between the 2D FM SLs in the $(MnBi_2Te_4)(Bi_2Te_3)_m$ series is AFM for $m = 0$, 1, 2 ($MnBi_2Te_4$, $MnBi_4Te_7$, and $MnBi_6Te_{10}$), FM for $m = 3$ ($MnBi_8Te_{13}$) and then progressively weakens with increase of m ($MnBi_{10}Te_{16}$, $MnBi_{12}Te_{19}$, and $MnBi_{14}Te_{22}$). As we show next, these crossovers have profound consequences for the topological properties of the materials in this series.

TOPOLOGICAL SURFACE STATES

We now turn to the electronic structure study of the compounds in the $(MnBi_2Te_4)(Bi_2Te_3)_m$ series. As it has been mentioned above, the $MnBi_2Te_4$ ($m = 0$) compound was shown to be an AFM TI. The ARPES dispersion relations for the (0001) surface of the $MnBi_4Te_7$ compound ($m = 1$) measured at $T = 60$ K are shown in Fig. 2a. Within the binding energy (BE) window from 0.5 to 4 eV, a quite complex bandstructure, characteristic of bismuth chalcogenides is seen[46,47]. However, unlike nonmagnetic TIs, a weakly dispersing state is discernible in Fig. 2a at the BE of about 3.8 eV, which is attributed to the Mn 3d-states, whose intensity is enhanced at the Mn-resonant photon energy of 50 eV.

Detailed ARPES dispersion relations in the low-energy part of the spectrum are presented in Fig. 2b ($h\nu = 30$ eV). Around the $\bar{\Gamma}$-point, there are two electron pockets that can be attributed to the bulk conduction bands of $MnBi_4Te_7$. Thus the material is n-doped which is typical of Bi-containing TIs[48]. The third electronic band, crossing the Fermi level, has largely a linear dispersion except for the close vicinity of the $\bar{\Gamma}$-point, where it becomes practically flat at the BE of 0.27 eV. At slightly higher BE, there is a M-shaped state, which is accompanied by a hole-like band with which it is degenerate at the Brillouin zone (BZ) center. Thus, between the linear and M-shaped states there is a band gap. Below the gap the electron-like part of the latter band behaves like a continuation of the linear band, as both have practically the same group velocity.

To separate the bulk and surface states, ARPES measurements with various photon energies (50, 18, and 6.3 eV (laser)) have been performed, as presented in Supplementary Fig. 6. The dispersion of the linear band does not show any photon energy dependence, which points towards its surface or 2D character. This allows suggesting that the linear band is the TSS, while far from the $\bar{\Gamma}$-point the M-shaped band is likely to be the trivial surface state in the valence band that interacts with the TSS near the $\bar{\Gamma}$-point, leading to the appearance of the "avoided crossing" gap at the BE of 0.29 eV. In this case, the degeneracy point between the M-band and the close-lying hole band can be identified as the Dirac point (DP) of the $MnBi_4Te_7$(0001) TSS.

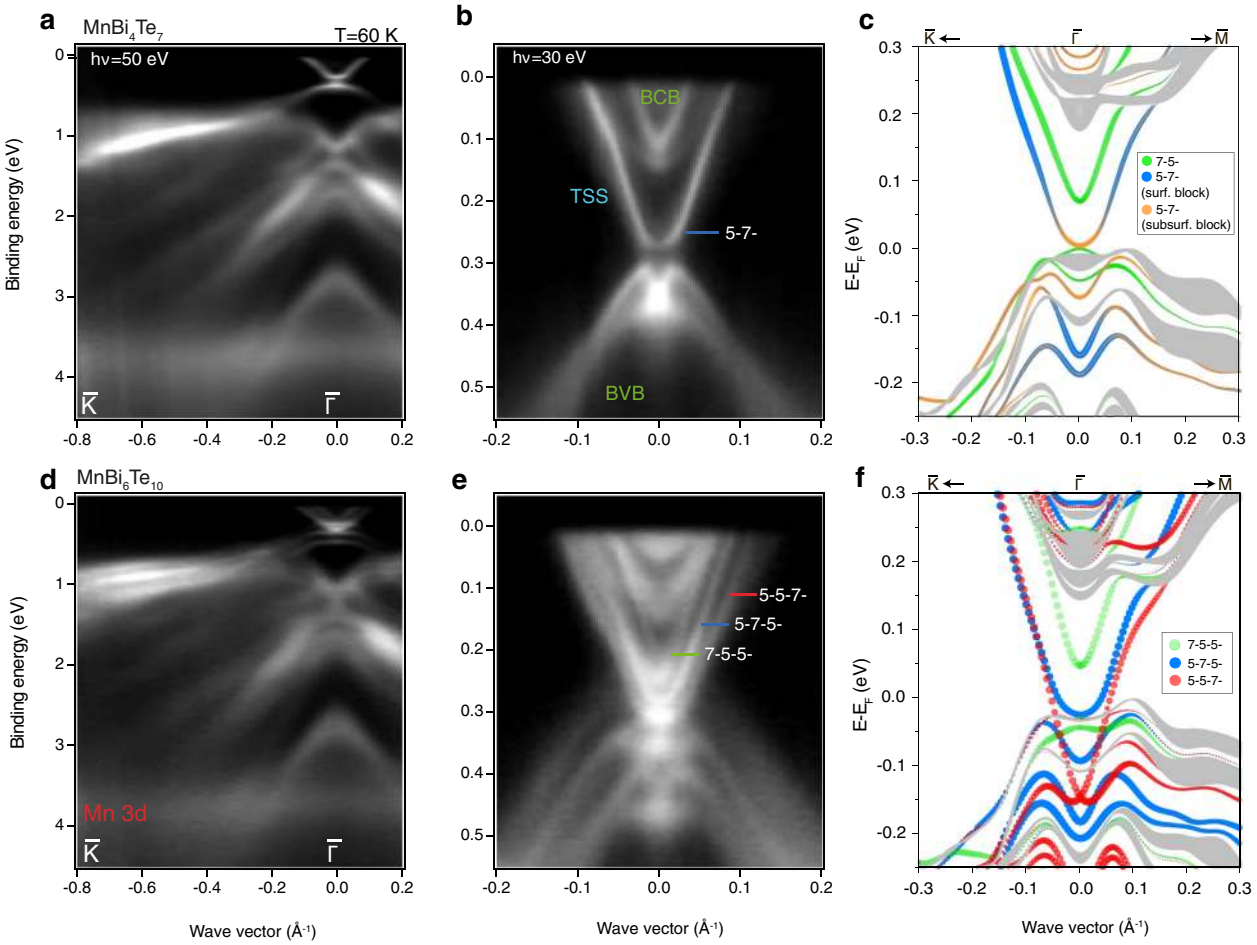

Fig. 2 **a**, **d** ARPES dispersion relations for the large energy and momentum region of $MnBi_4Te_7$ and $MnBi_6Te_{10}$ taken at 60 K at a photon energy of 50 eV. **b, e** ARPES dispersion relations of the Dirac cone region taken at a photon energy of 30 eV at 60 K (BCB (BVB) denotes bulk conduction (valence) band). **c** DFT-calculated layer-resolved electronic structure of the $MnBi_4Te_7$(0001) surface. The size of color circles reflects the weight of the state in the topmost block of the SL (green) and QL (blue) termination. The orange circles show the contribution of the subsurface SL block of the QL termination. The gray shadings correspond to the bulk bandstructure projected onto the 2D Brillouin zone. **f** The same for $MnBi_6Te_{10}$(0001) surface, the size of green, blue, and red circles reflects the weight of the state in the topmost block of the 7-5-5-, 5-7-5-, and 5-5-7- terminations, respectively.

Since the TSS should be spin-polarized, spin-ARPES measurements have been performed. The acquired spectra (Supplementary Fig. 6) clearly demonstrate the spin polarization reversal for opposite branches of the linear band, revealing the characteristic helical spin texture of the TSS. The performed bands assignment allows us to estimate the bulk band gap of $MnBi_4Te_7$ to be about 0.15 eV. It should be noted that on the surface of $MnBi_4Te_7$, since it is built of two different crystal blocks, QL and SL, two surface terminations and, consequently, two Dirac TSSs with different dispersion are expected. The TSS signal for each termination has been obtained by means of laser-ARPES and will be analyzed below.

According to the DFT electronic structure calculations, AFM bulk $MnBi_4Te_7$ features a fundamental band gap of 0.18 eV (Supplementary Note 3). Because of its interlayer AFM ordering, $MnBi_4Te_7$ is invariant with respect to the combination of the time-reversal (Θ) and primitive-lattice translation ($T_{1/2}$) symmetries, $S = \Theta T_{1/2}$, and thus obeys the Z_2 topological classification of AFM insulators[24,49]. We find $Z_2 = 1$ for $MnBi_4Te_7$, meaning that its fundamental band gap is inverted whereby, similarly to $MnBi_2Te_4$, $MnBi_4Te_7$ is an AFM TI below the Néel temperature. The AFM TI state of $MnBi_4Te_7$ along with the out-of-plane direction of the staggered magnetization's easy axis dictate that there should be a gapped (gapless) TSS at the *S*-breaking (*S*-preserving) surface. This is exactly what we find: the TSS is gapped at both of the possible terminations of the $MnBi_4Te_7$(0001) surface, which is *S*-breaking. At the SL termination, the DP gap is located inside the fundamental bulk band gap and reaches a large value of 70 meV (Fig. 2c). At the QL termination, a more complex surface electronic structure is revealed, with four bands located in the region of interest. To understand this spectrum, we have performed surface electronic structure calculations at different spin–orbit coupling (SOC) strengths. As it can be seen in Supplementary Fig. 10, with no SOC included there is an exchange-split trivial surface state in the valence band's projected band gap around the $\bar{\Gamma}$-point at energy of about −0.3 eV. When the SOC is turned on and the system is in the topological phase, this spin-split state interacts with the TSS of the QL-termination, leading to the appearance of avoided crossings (Supplementary Fig. 10).

At the natural SOC strength (Fig. 2c), these avoided crossing effects are quite significant and the Dirac cone appears to be torn into two parts, one of which is located in the fundamental band gap, while another in the projected band gap between approximately −0.1 and −0.2 eV. The split DP of the QL termination lies at about 0.16 eV below the Fermi level. The smaller DP gap size at the QL termination (about 29 meV) is caused by the predominant localization of the TSS in the surface

block, whereby the interaction of this state with the Mn layer, lying in the subsurface block, is weaker. Thus, the complex dispersion of the QL-termination TSS is caused by the interaction with the trivial surface state, located in the bulk valence band (BVB).

A comparison between the experimental and theoretical spectra allows identifying the measured surface bandstructure in Fig. 2b as that of the QL termination. In the PM state, the trivial surface state is exchange-unsplit which leads to a less complex appearance of the overall spectrum (as compared to the theoretical one): there is only one avoided crossing clearly seen in ARPES in Fig. 2b. Thus, the gap in the TSS at a BE of about 0.27 eV (Fig. 2b) is indeed related to the "cut" of the Dirac cone by a trivial surface state and therefore this gap is observed above the Néel temperature. Cooling down below the magnetic critical point does not lead to significant changes (see Supplementary Fig. 7), except for a slight broadening of the BVB, most likely related to the exchange splitting of the bulk states. Finally, our tight-binding calculations of the *S*-preserving $(10\bar{1}1)$ surface electronic structure reveal a gapless TSS, as expected for an AFM TI (see Supplementary Fig. 4).

The TSSs are also observed for the next member in $(MnBi_2Te_4)(Bi_2Te_3)_m$ series, $MnBi_6Te_{10}$ ($m = 2$). The ARPES dispersion relations for this compound are shown in Fig. 2d, measured at the same conditions as the spectrum in Fig. 2a. In the BE region from 1 to 5 eV, the valence band dispersions for $MnBi_6Te_{10}$ look similar to those of $MnBi_4Te_7$. Apparently, the intensity of the Mn-3*d* resonant feature seen at the BE of 3.8 eV is slightly decreased for $MnBi_6Te_{10}$, in accordance with the lower relative Mn concentration. The most pronounced difference between the band structures of the two compounds takes place in the region of BE between 1 eV and E_F, where the surface states dominate the photoemission signal. In particular, in Fig. 2d one can see three weakly dispersing states along the $\bar{\Gamma} - \bar{K}$ direction around the BE of 1 eV as well as three Dirac cones at the BZ center. This complex dispersion of the TSSs is resolved in the detailed ARPES image, shown in Fig. 2e, where both the lower and upper parts of the three Dirac cones can be clearly seen.

The appearance of three TSSs at the $MnBi_6Te_{10}(0001)$ surface is caused by the peculiar crystal structure of the ($m = 2$) compound, built of the two types of blocks, stacked on top of each other in the -5-5-7-5-5-7- sequence. In such a case, the cleavage procedure leads to the formation of different surface terminations. Such a structure was previously observed for the $PbBi_6Te_{10}(0001)$ surface, where the three terraces were attributed to the 5-5-7-, 5-7-5- and 7-5-5- terminations, showing different dispersions of the TSS[50]. Similarly to $PbBi_6Te_{10}$, the cleaved surface of $MnBi_6Te_{10}$ may exhibit three types of terminations, two of them having a QL on the surface (i.e. either 5-5-7- or 5-7-5-), while the third possible crystal truncation is that by the SL (7-5-5-). Similarly to the $PbBi_6Te_{10}$ case, these terraces have different Dirac cone-binding energies. The inner Dirac state (which by analogy with non-magnetic TIs with similar structure can be assigned to the TSS generated by the SL-terminated terraces) shows the lowest BE of the DP which is located above the BVB states, while the other two cones (coming from different QL terraces) overlap with the BVB. Measurements at low temperature (1 K, Supplementary Fig. 9) exhibit some changes in the ARPES spectra due to magnetic ordering, that could be related to the gap appearance in the Dirac cone of the SL termination, similar to ref. [51].

Similarly to $MnBi_4Te_7$, the AFM $MnBi_6Te_{10}$ obeys the combined $S = \Theta T_{1/2}$-symmetry and based on our DFT calculations we classify it as an AFM TI with a bulk band gap of about 0.145 eV. The DFT-calculated (0001) surface band structure of the AFM $MnBi_6Te_{10}$ is presented in Fig. 2f, where three Dirac cones are clearly seen in agreement with the ARPES data. Both the 7-5-5- and 5-7-5-terminations show essentially similar behaviors to those revealed for the $MnBi_4Te_7(0001)$. The TSS of the 5-5-7- termination is mostly located in the surface QL block and therefore its DP is almost unsplit.

In order to experimentally separate various terminations of $MnBi_4Te_7$ and $MnBi_6Te_{10}$, we used laser-based ARPES technique that spatial resolution is up to ~5 μm[52], while for synchrotron-based measurements (Fig. 2) the resolution is up to ~100 μm. In Fig. 3 the corresponding dispersion relations are presented for two (upper panels) and three (lower panels) terminations of $MnBi_4Te_7$ and $MnBi_6Te_{10}$, respectively. In contrast to the synchrotron-based measurements the SL-terminated Dirac cone for $MnBi_4Te_7$ has been revealed (Fig. 3a). Spectra from QL terminated surfaces (5-7-, 5-7-5- and 5-5-7- (see Fig. 3b, e, f), correspondingly) are in good agreement with theoretical predictions and synchrotron measurements (see Fig. 2), as well as with the recent experimental works[53–55]. The distinct DP positions can be easily determined for 5-7-5- and 5-5-7- terminations of $MnBi_6Te_{10}$, which has larger BE for 5-7-5- termination, in accordance with the theory.

The electronic structure of SL terminated surfaces of $MnBi_4Te_7$ and $MnBi_6Te_{10}$ (Fig. 3a, d) have similar features and the most important is the Dirac cone, located within the bulk band gap, with the DP at ≃0.28 eV of BE, in agreement with the DFT-derived band structure (Fig. 2c, f). Nevertheless, besides the Dirac cone and bulk bands the laser-based spectra exhibit the wide parabolic-like state, dispersing from ~0.25 eV at the $\bar{\Gamma}$-point to the Fermi level at ~0.17 $Å^{-1}$, that is absent in ab initio calculations (see Fig. 2c, f and refs. [53,56,57]). Similar band dispersions for SL-terminated terrace have been observed in refs. [54,56,57]. The origin of the parabolic-like band is under debates currently. Since ab initio calculations cannot reproduce this electronic band, its origin can lie in the deviations of the surface structure from the ideal one. As an example, recently the dramatic effect of small variation of the near surface vdW gap on the band structure of $MnBi_2Te_4(0001)$ has been demonstrated[58]. In refs. [56,57] the idea of Rashba-like surface state on SL-termination is proposed. Indeed, surface localization of the band can be confirmed since it exists only in SL-terminations and it does not appear for QL-terminated surfaces (Fig. 3b, e, and f). The ARPES Fermi surface (Fig. 3c) exhibits a weak hexagonal warping of the band and absence of the interaction with the bulk conduction band states. Notably, similar band was not observed for SL-terminated surfaces in structurally similar compounds $PbBi_4Te_7$ and $PbBi_6Te_{10}$[50,59]. One also can notice that spectra for SL-termination in $MnBi_4Te_7$ and $MnBi_6Te_{10}$ slightly differ in the valence band region, where interaction of the lower part of the Dirac cone with the bulk bands is seen for the case of $MnBi_6Te_{10}$.

Finally, the electronic structure measurements performed for the $MnBi_8Te_{13}(0001)$ and $MnBi_{10}Te_{16}(0001)$ surfaces reveal the presence of the TSSs within the bulk band gap too (see Supplementary Figure 5), but their analysis is complicated due to increased number of surface terraces after the cleavage.

Thus, all the compounds of the presented $(MnBi_2Te_4)(Bi_2Te_3)_m$ family are magnetic TIs, whose topological class changes with *m*. While $MnBi_2Te_4$, $MnBi_4Te_7$, and $MnBi_6Te_{10}$ ($m = 0, 1, 2$) are 3D AFM TIs, $MnBi_8Te_{13}$ ($m = 3$) turns out to be a FM TI with weak interlayer exchange coupling. For $m > 3$ no signatures of the interlayer exchange interaction could be detected in our experiments, which has a very interesting consequence: $MnBi_{10}Te_{16}$, $MnBi_{12}Te_{19}$, and $MnBi_{14}Te_{22}$ could be the first examples of stoichiometric 3D MTI compounds in which the magnetizations of the 2D FM-ordered layers are disordered along the [0001] direction below the corresponding critical temperature. Similar idea has been discussed in ref. [60] where starting from $m = 3$ the so-called "single layer magnet" phase is proposed.

The peculiar magnetic properties of the $(MnBi_2Te_4)(Bi_2Te_3)_m$ family combined with the nontrivial topology of its constituents enable observation of interesting effects for all of the presented members of the series. Those effects would take advantage of the interlayer exchange coupling tunability along the series, which is

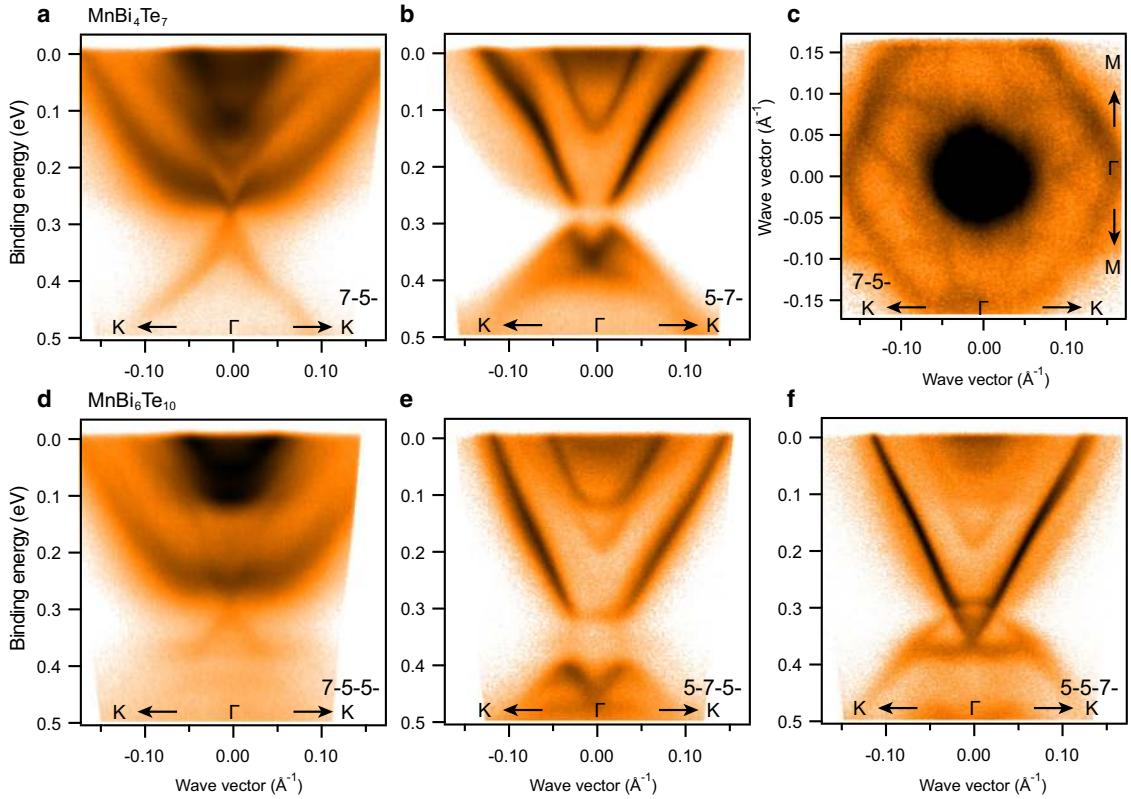

Fig. 3 **a**, **b** Laser-based ARPES dispersion relations of indicated terminations of $MnBi_4Te_7$ along $\overline{K}-\overline{\Gamma}-\overline{K}$ direction of the Brillouin zone and **c** the Fermi surface of 7-5- termination taken at 15 K at a photon energy of 6.3 eV. **d**–**f** Laser-based ARPES dispersion relations of various terminations of $MnBi_6Te_{10}$ taken at the same conditions as **a**, **b**.

feasible through the changing of the number of QLs separating the SLs. This allows one to tailor both the strength and character of the interlayer exchange coupling and even to switch it off for large m numbers. One particular consequence of it is that the magnetic structure, and therefore the topological class of the compounds can be tuned by an external magnetic field. This property is especially attractive in the 2D limit, where the $[MnBi_2Te_4]_{1SL}/(Bi_2Te_3)_{mQL(s)}/[MnBi_2Te_4]_{1SL}$ sandwiches, that can be obtained by careful exfoliation of the thin flakes from the single crystal surface[31,32], turn to either the intrinsic zero plateau QAH state (also known as the axion insulator state) or the Chern insulator state. For $m > 3$, the latter state can be achieved in zero external magnetic field as has been earlier predicted by theory[20], while for $MnBi_2Te_4$ and, probably, for $MnBi_4Te_7$ an external magnetic field is needed to achieve the quantized Hall effect[31,32]. However, in the $MnBi_4Te_7$ and $MnBi_6Te_{10}$ compounds, the strength of the critical field needed to overcome the AFM interlayer exchange coupling should be much smaller than that used for $MnBi_2Te_4$. The latter fact has also been pointed out as an advantage for a possible realization of the topological superconductor state based on the $(MnBi_2Te_4)(Bi_2Te_3)_m$ family, hosting the exotic Majorana fermions[33]. From this point of view, the $(MnBi_2Te_4)(Bi_2Te_3)_m$ series represents a unique and highly tunable topological van-der-Waals platform for creation of both exotic topological phases and functional devices for AFM and 2D spintronics as well as for topological quantum computing.

In summary, we have reported the magnetic topological insulators (MTIs) family $(MnBi_2Te_4)(Bi_2Te_3)_m$ consisting of Mn-based magnetic SL blocks separated by different number m of non-magnetic quintuple layers. The interlayer exchange coupling between the neighboring SLs can be tuned by changing m giving rise to a crossover from the interlayer AFM ordering for $m = 0$, 1, 2 ($MnBi_2Te_4$, $MnBi_4Te_7$, and $MnBi_6Te_{10}$) to the overall ferromagnetic one for $m = 3$ ($MnBi_8Te_{13}$) and, finally, to almost complete disappearance of the interlayer interaction for $m > 3$ ($MnBi_{10}Te_{16}$, $MnBi_{12}Te_{19}$, and $MnBi_{14}Te_{22}$). Combined with a non-trivial topology of the $(MnBi_2Te_4)(Bi_2Te_3)_m$ compounds, proven by ARPES, these magnetic states give rise to the AFM and FM TI phases for $m = 0$, 1, 2 and $m = 3$, respectively, while for $m > 3$ a new MTI phase could be formed in which, below T_C, the magnetizations of the 2D FM-ordered Mn layers of the $MnBi_2Te_4$ building blocks are disordered along the [0001] direction. Depending on the surface terminations, a complex bundle of the Dirac cones is resolved by means of DFT and ARPES. The tunable magnetic and topological phases in $(MnBi_2Te_4)(Bi_2Te_3)_m$ series allow engineering the promising platforms not only for QAH effect, axion insulators, and Majorana fermions, but also for emerging fields of AFM and van-der-Waals 2D spintronics.

METHODS

Magnetic and transport measurements

Magnetic measurements were carried out in the resource center "Center for Diagnostics of Materials for Medicine, Pharmacology and Nanoelectronics" of the SPbU Science Park using a SQUID magnetometer with a helium cryostat manufactured by Quantum Design. The experiments were carried out in a pull mode in terms of temperature and magnetic field. The applied magnetic field was perpendicular to the (0001) sample surface. Transport measurements were done with a standard four-probe ac technique using a low-frequency ($f \propto 20$ Hz) Lock-in amplifier. Contacts were attached with conducting graphite paste. The experiments were carried out in a temperature-variable cryostat at different values of magnetic field up to 8 T, generated by a superconducting solenoid and directed along the normal to the (0001) sample surface.

Photoemission measurements

The experiments were carried out at 1-cubed UE-112 beamline at BESSY II in Berlin, BaDElPh beamline[61] at Elettra synchrotron in Trieste (Italy), BL-1, BL-9, and laser ARPES endstation at HiSOR in Hiroshima, and at Research Resource Center of Saint Petersburg State University "Physical methods of surface investigation" with a Scienta R4000 or a Specs Phoibos 150 energy analyzer. Samples were cleaved in situ at the base pressure of 6×10^{-11} mbar. The crystalline order and cleanliness of the surface were checked by low-energy electron diffraction (LEED) and X-ray photoelectron spectroscopy (XPS). Spin-resolved ARPES measurements were performed at BL-9 beamline of HiSOR synchrotron in Hiroshima and APE beamline at Elettra synchrotron in Trieste (Italy). The spectra were measured using VLEED spin detector. Total energy and angular resolutions were 20 meV and 1.5°, respectively.

Electronic structure and total energy calculations

Electronic structure calculations were performed using the density functional theory and the projector-augmented wave (PAW) method[62], realized in the VASP code[63,64]. The exchange-correlation potential was described within the generalized gradient approximation in the Perdew–Burke–Ernzerhof formulation (GGA-PBE)[65]. The Hamiltonian contained scalar relativistic corrections and the SOC was taken into account self-consistently[66]. We used the DFT-D2[67] and the DFT-D3[68,69] approaches to describe the vdW interactions, that yielded similar results. The plane-waves with energies up to 270 eV were used for the wave functions expansion. Structural relaxations were done until the forces on atoms were smaller than 0.01 eV/Å. Depending on the particular task and geometry, different grids for the BZs sampling were used (see below), all of them being $\bar{\Gamma}$-centered.

The Mn 3*d*-states were described using the GGA + *U* method[70] as formulated by Dudarev et al.[71]. The $U_{\mathrm{eff}} = U - J$ value for the Mn 3*d*-states was chosen to be equal to 5.34 eV, as in previous works on $MnBi_2Te_4$[19–21,25,26,72].

The bulk magnetic ordering was studied using total-energy calculations, performed for the FM and two different AFM states. Namely, we considered an interlayer AFM state and a noncollinear (NCL) intralayer AFM state, in which three spin sublattices form angles of 120° with respect to each other[72]. To model the FM and interlayer AFM structures in $MnBi_4Te_7$ and $MnBi_6Te_{10}$, we used cells with 24 and 34 atoms, respectively. For the $MnBi_4Te_7$ system, these calculations were performed with the respective 3D BZs sampled by the $25 \times 25 \times 5$*k*-point grids. For the $MnBi_6Te_{10}$ compound, which exhibits extremely weak interlayer exchange coupling, the interlayer ordering was carefully studied using very fine *k*-meshes up to $23 \times 23 \times 19$ points. These meshes were also used in the magnetic anisotropy energy calculations. For $MnBi_4Te_7$, the NCL intralayer AFM configuration was treated using hexagonal bulk cell containing three atoms per layer [$(\sqrt{3} \times \sqrt{3})R30°$ in-plane periodicity] and a $11 \times 11 \times 3$ BZ sampling. For $MnBi_6Te_{10}$, NCL configuration has not been considered since all the available experimental and theoretical data in the literature indicate that each $MnBi_2Te_4$ SL block orders ferromagnetically, irrespectively of its structural environment.

The $MnBi_4Te_7$ and $MnBi_6Te_{10}$ semi-infinite surfaces were simulated within a model of repeating slabs separated by a vacuum gap of at least 10 Å. The interplanar distances were optimized for the utmost SL or QL block of each surface. The structural relaxations and static electronic structure calculations were performed using a *k*-point mesh of $11 \times 11 \times 1$ in the 2D BZ.

The procedures of the magnetic anisotropy energy calculations and Monte Carlos simulations are described in detail in ref. [25].

Exchange coupling constants calculations

For the equilibrium atomic structure of $MnBi_4Te_7$ obtained with VASP, we calculated the Heisenberg exchange coupling constants $J_{0,i}$ ab initio using the full-potential linearized augmented plane waves (FLAPW) method[73] in the FLEUR implementation (http://www.flapw.de). In the $J_{0,i}$ calculations SOC was neglected. We took the GGA+*U* approach[74,75] under the fully localized limit[76], using similar settings as those in refs. [25,26]. For the self-consistent FLAPW basis set, the plane waves were constructed with a $18 \times 18 \times 4$ Monkhorst–Pack *k*-point sampling of the first BZ and cut-off energies of 3.4 Hartrees for the wavefunctions and 10.4 Hartrees for the density and potential expansions. Muffin tin sphere radius was set to 2.74 a.u., for Mn, while a value of 2.81 a.u. was used for Bi and Te, and the partial wave functions were expanded up to $l = 8$. Mn, Bi, and Te contributed 4*s*3*d*, 5*s*5*p*, and 6*s*6*p* valence electrons, respectively.

The $J_{0,i}$ constants were extracted by Fourier inversion of spin spirals in the reciprocal cell characterized by the *q* vectors of a $19 \times 19 \times 3$ grid. These dispersion energies, calculated in the force theorem approach, converged below 0.1 meV and allowed adding up to 150 magnetic coordination spheres to the Fourier analysis.

DATA AVAILABILITY

The data that support the findings of this study are available from the corresponding author upon reasonable request.

Received: 24 January 2020; Accepted: 2 July 2020;
Published online: 03 August 2020

REFERENCES

1. Liu, C.-X., Qi, X.-L., Dai, X., Fang, Z. & Zhang, S.-C. Quantum anomalous Hall effect in $Hg_{1-y}Mn_yTe$ quantum wells. *Phys. Rev. Lett.* **101**, 146802 (2008).
2. He, K., Wang, Y. & Xue, Q.-K. Quantum anomalous Hall effect. *Natl Sci. Rev.* **1**, 38–40 (2014).
3. Chang, C.-Z. et al. Experimental observation of the quantum anomalous Hall effect in a magnetic topological insulator. *Science* **340**, 167–170 (2013).
4. Chang, C.-Z. et al. High-precision realization of robust quantum anomalous Hall state in a hard ferromagnetic topological insulator. *Nat. Mater.* **14**, 473–477 (2015).
5. Feng, Y. et al. Observation of the zero Hall plateau in a quantum anomalous Hall insulator. *Phys. Rev. Lett.* **115**, 126801 (2015).
6. Gibertini, M., Koperski, M., Morpurgo, A. F. & Novoselov, K. S. Magnetic 2D materials and heterostructures. *Nat. Nanotechnol.* **14**, 408–419 (2019).
7. Burch, K. S., Mandrus, D. & Park, J.-G. Magnetism in two-dimensional van der Waals materials. *Nature* **563**, 47–52 (2018).
8. Lin, X., Yang, W., Wang, K. L. & Zhao, W. Two-dimensional spintronics for low-power electronics. *Nat. Electron.* **2**, 274–283 (2019).
9. Jungwirth, T., Marti, X., Wadley, P. & Wunderlich, J. Antiferromagnetic spintronics. *Nat. Nanotechnol.* **11**, 231–241 (2016).
10. Šmejkal, L., Mokrousov, Y., Yan, B. & MacDonald, A. H. Topological antiferromagnetic spintronics. *Nat. Phys.* **14**, 242–251 (2018).
11. Baltz, V. et al. Antiferromagnetic spintronics. *Rev. Mod. Phys.* **90**, 015005 (2018).
12. Checkelsky, J. G., Ye, J., Onose, Y., Iwasa, Y. & Tokura, Y. Dirac-fermion-mediated ferromagnetism in a topological insulator. *Nat. Phys.* **8**, 729–733 (2012).
13. Chen, Y. L. et al. Massive Dirac fermion on the surface of a magnetically doped topological insulator. *Science* **329**, 659–662 (2010).
14. Henk, J. et al. Complex spin texture in the pure and Mn-doped topological insulator Bi_2Te_3. *Phys. Rev. Lett.* **108**, 206801 (2012).
15. Hor, Y. S. et al. Development of ferromagnetism in the doped topological insulator $Bi_{2-x}Mn_xTe_3$. *Phys. Rev. B* **81**, 195203 (2010).
16. Shikin, A. M. et al. Signatures of in-plane and out-of-plane magnetization generated by synchrotron radiation in magnetically doped and pristine topological insulators. *Phys. Rev. B* **97**, 245407 (2018).
17. Eremeev, S. V., Men'shov, V. N., Tugushev, V. V., Echenique, P. M. & Chulkov, E. V. Magnetic proximity effect at the three-dimensional topological insulator/magnetic insulator interface. *Phys. Rev. B* **88**, 144430 (2013).
18. Katmis, F. et al. A high-temperature ferromagnetic topological insulating phase by proximity coupling. *Nature* **533**, 513 EP – (2016).
19. Otrokov, M. M. et al. Magnetic extension as an efficient method for realizing the quantum anomalous Hall state in topological insulators. *JETP Lett.* **105**, 297–302 (2017).
20. Otrokov, M. M. et al. Highly-ordered wide bandgap materials for quantized anomalous Hall and magnetoelectric effects. *2D Mater.* **4**, 025082 (2017).
21. Hirahara, T. et al. Large-gap magnetic topological heterostructure formed by subsurface incorporation of a ferromagnetic layer. *Nano Lett.* **17**, 3493–3500 (2017).
22. Eremeev, S. V., Otrokov, M. M. & Chulkov, E. V. New universal type of interface in the magnetic insulator/topological insulator heterostructures. *Nano Lett.* **18**, 6521–6529 (2018).
23. Rienks, E. D. L. et al. Large magnetic gap at the Dirac point in Bi2Te3/MnBi2Te4 heterostructures. *Nature* **576**, 423–428 (2019).
24. Mong, R. S. K., Essin, A. M. & Moore, J. E. Antiferromagnetic topological insulators. *Phys. Rev. B* **81**, 245209 (2010).
25. Otrokov, M. M. et al. Prediction and observation of an antiferromagnetic topological insulator. *Nature* **576**, 416–422 (2019).
26. Otrokov, M. M. et al. Unique thickness-dependent properties of the van der waals interlayer antiferromagnet $MnBi_2Te_4$ films. *Phys. Rev. Lett.* **122**, 107202 (2019).

27. Zhang, D. et al. Topological axion states in the magnetic insulator $MnBi_2Te_4$ with the quantized magnetoelectric effect. *Phys. Rev. Lett.* **122**, 206401 (2019).
28. Li, J. et al. Intrinsic magnetic topological insulators in van der Waals layered MnBi2Te4-family materials. *Sci. Adv.* **5**, eaaw5685 (2019).
29. Gong, Y. et al. Experimental realization of an intrinsic magnetic topological insulator. *Chin. Phys. Lett.* **36**, 076801 (2019).
30. Peng, Y. & Xu, Y. Proximity-induced Majorana hinge modes in antiferromagnetic topological insulators. *Phys. Rev. B* **99**, 195431 (2019).
31. Deng, Y. et al. Quantum anomalous Hall effect in intrinsic magnetic topological insulator MnBi2Te4. *Science* **367**, 895–900 (2020).
32. Liu, C. et al. Robust axion insulator and chern insulator phases in a two-dimensional antiferromagnetic topological insulator. *Nat. Mater.* **19**, 522–527 (2020).
33. Zhang, J., Liu, Z. & Wang, J. In-plane magnetic-field-induced quantum anomalous hall plateau transition. *Phys. Rev. B* **100**, 165117 (2019).
34. Zhang, J. et al. Dynamical magnetoelectric effect in antiferromagnetic insulator $Mn_2Bi_2Te_5$. Preprint at https://arxiv.org/abs/1906.07891 (2019).
35. Zhang, R.-X., Wu, F. & Das Sarma, S. Möbius insulator and higher-order topology in $MnBi_{2n}Te_{3n+1}$. *Phys. Rev. Lett.* **124**, 136407 (2020).
36. Estyunin, D. A. et al. Signatures of temperature driven antiferromagnetic transition in the electronic structure of topological insulator $MnBi_2Te_4$. *APL Mater.* **8**, 021105 (2020).
37. Yan, J.-Q. et al. Crystal growth and magnetic structure of $MnBi_2Te_4$. *Phys. Rev. Mater.* **3**, 064202 (2019).
38. Aliev, Z. S. et al. Novel ternary layered manganese bismuth tellurides of the MnTe–Bi_2Te_3 system: synthesis and crystal structure. *J. Alloy. Compd.* **789**, 443–450 (2019).
39. Sun, H. et al. Rational design principles of the quantum anomalous Hall effect in superlatticelike magnetic topological insulators. *Phys. Rev. Lett.* **123**, 096401 (2019).
40. Hu, C. et al. A van der Waals antiferromagnetic topological insulator with weak interlayer magnetic coupling. *Nat. Commun.* **11**, 97 (2020).
41. Wu, J. et al. Natural van der Waals heterostructural single crystals with both magnetic and topological properties. *Sci. Adv.* **5**, eaax9989 (2019).
42. Vidal, R. C. et al. Topological electronic structure and intrinsic magnetization in $MnBi_4Te_7$: a Bi_2Te_3 derivative with a periodic Mn sublattice. *Phys. Rev. X* **9**, 041065 (2019).
43. Yan, J.-Q. et al. A-type antiferromagnetic order in $MnBi_4Te_7$ and $MnBi_6Te_{10}$ single crystals. *Phys. Rev. Mater.* **4**, 054202 (2020).
44. Hu, C. et al. Realization of an intrinsic, ferromagnetic axion insulator in MnBi8Te13. Preprint at https://arxiv.org/abs/1910.12847 (2019).
45. Liang, Z. et al. Mapping the Dirac fermions in intrinsic antiferromagnetic topological insulators $(MnBi_2Te_4)(Bi_2Te_3)_n$ ($n = 0$, 1). Preprint at https://arxiv.org/abs/2001.00866 (2020).
46. Shikin, A. M. et al. Electronic and spin structure of the topological insulator $Bi_2Te_{2.4}Se_{0.6}$. *Phys. Rev. B* **89**, 125416 (2014).
47. Bansil, A., Lin, H. & Das, T. Colloquium: topological band theory. *Rev. Mod. Phys.* **88**, 021004 (2016).
48. Hasan, M. Z. & Kane, C. L. Colloquium: topological insulators. *Rev. Mod. Phys.* **82**, 3045–3067 (2010).
49. Fang, C., Gilbert, M. J. & Bernevig, B. A. Topological insulators with commensurate antiferromagnetism. *Phys. Rev. B* **88**, 085406 (2013).
50. Papagno, M. et al. Multiple coexisting Dirac surface states in three-dimensional topological insulator $PbBi_6Te_{10}$. *ACS Nano* **10**, 3518–3524 (2016).
51. Jo, N. H. et al. Intrinsic axion insulating behavior in antiferromagnetic $MnBi_6Te_{10}$. Preprint at https://arxiv.org/abs/1910.14626 (2019).
52. Iwasawa, H. et al. Development of laser-based scanning μ-arpes system with ultimate energy and momentum resolutions. *Ultramicroscopy* **182**, 85–91 (2017).
53. Gordon, K. N. et al. Strongly gapped topological surface states on protected surfaces of antiferromagnetic $MnBi_4Te_7$ and $MnBi_6Te_{10}$. Preprint at https://arxiv.org/abs/1910.13943 (2019).
54. Xu, L. X. et al. Persistent gapless surface states in MnBi2Te4/Bi2Te3 superlattice antiferromagnetic topological insulator. Preprint at https://arxiv.org/abs/1910.11014 (2019).
55. Hu, Y. et al. Universal gapless Dirac cone and tunable topological states in $(MnBi_2Te_4)_m(Bi_2Te_3)_n$ heterostructures. *Phys. Rev. B* **101**, 161113 (2020).
56. Wu, X. et al. Distinct topological surface states on the two terminations of $MnBi_4Te_7$. *Phys. Rev. X* **10**, 031013 (2020).
57. Ma, X.-M. et al. Hybridization-induced gapped and gapless states on the surfaces of magnetic topological insulators. Preprint at https://arxiv.org/abs/1912.13237 (2019).
58. Shikin, A. M. et al. Nature of the Dirac gap modulation and surface magnetic interaction in axion antiferromagnetic topological insulator $MnBi_2Te_4$. Preprint at https://arxiv.org/abs/2004.04802 (2020).
59. Eremeev, S. V. et al. Atom-specific spin mapping and buried topological states in a homologous series of topological insulators. *Nat. Commun.* **3**, 635 (2012).
60. Wu, J. et al. Toward 2D magnets in the $(MnBi_2Te_4)(Bi_2Te_3)n$ bulk crystal. *Adv. Mater.* **32**, 2001815 (2020).
61. Petaccia, L. et al. BaD ElPh: a 4 m normal-incidence monochromator beamline at Elettra. *Nucl. Instrum. Methods Phys. Res. A* **606**, 780–784 (2009).
62. Blöchl, P. E. Projector augmented-wave method. *Phys. Rev. B* **50**, 17953–17979 (1994).
63. Kresse, G. & Furthmüller, J. Efficient iterative schemes for ab initio total-energy calculations using a plane-wave basis set. *Phys. Rev. B* **54**, 11169–11186 (1996).
64. Kresse, G. & Joubert, D. From ultrasoft pseudopotentials to the projector augmented-wave method. *Phys. Rev. B* **59**, 1758–1775 (1999).
65. Perdew, J. P., Burke, K. & Ernzerhof, M. Generalized gradient approximation made simple. *Phys. Rev. Lett.* **77**, 3865–3868 (1996).
66. Koelling, D. D. & Harmon, B. N. A technique for relativistic spin-polarised calculations. *J. Phys. C* **10**, 3107 (1977).
67. Grimme, S. Semiempirical GGA-type density functional constructed with a long-range dispersion correction. *J. Comput. Chem.* **27**, 1787–1799 (2006).
68. Grimme, S., Antony, J., Ehrlich, S. & Krieg, H. A consistent and accurate ab initio parametrization of density functional dispersion correction (DFT-D) for the 94 elements h-pu. *J. Chem. Phys.* **132**, 154104 (2010).
69. Grimme, S., Ehrlich, S. & Goerigk, L. Effect of the damping function in dispersion corrected density functional theory. *J. Comput. Chem.* **32**, 1456–1465 (2011).
70. Anisimov, V. I., Zaanen, J. & Andersen, O. K. Band theory and mott insulators: Hubbard *U* instead of stoner *I*. *Phys. Rev. B* **44**, 943–954 (1991).
71. Dudarev, S. L., Botton, G. A., Savrasov, S. Y., Humphreys, C. J. & Sutton, A. P. Electron-energy-loss spectra and the structural stability of nickel oxide: an LSDA +U study. *Phys. Rev. B* **57**, 1505–1509 (1998).
72. Eremeev, S. V., Otrokov, M. M. & Chulkov, E. V. Competing rhombohedral and monoclinic crystal structures in $MnPn_2Ch_4$ compounds: an ab-initio study. *J. Alloy. Compd.* **709**, 172–178 (2017).
73. Wimmer, E., Krakauer, H., Weinert, M. & Freeman, A. J. Full-potential self-consistent linearized-augmented-plane-wave method for calculating the electronic structure of molecules and surfaces: O_2 molecule. *Phys. Rev. B* **24**, 864–875 (1981).
74. Anisimov, V. I., Aryasetiawan, F. & Lichtenstein, A. I. First-principles calculations of the electronic structure and spectra of strongly correlated systems: the LDA+U method. *J. Phys. Condens. Matter* **9**, 767 (1997).
75. Shick, A. B., Liechtenstein, A. I. & Pickett, W. E. Implementation of the LDA+U method using the full-potential linearized augmented plane-wave basis. *Phys. Rev. B* **60**, 10763–10769 (1999).
76. Anisimov, V. I., Solovyev, I. V., Korotin, M. A., Czyżyk, M. T. & Sawatzky, G. A. Density-functional theory and NiO photoemission spectra. *Phys. Rev. B* **48**, 16929–16934 (1993).

ACKNOWLEDGEMENTS

This work is supported by Saint Petersburg State University project for scientific investigations (ID No. 51126254, https://spin.lab.spbu.ru) and Russian Science Foundation (Grant no. 18-12-00062 in part of the photoemission measurements and 18-12-00169 in part of calculations of topological invariants, investigation of dependence of the electronic spectra on SOC strength, and tight-binding band structure calculations). Russian Foundation for Basic Research (Grant nos. 20-32-70179 and 18-52-06009) and Science Development Foundation under the President of the Republic of Azerbaijan (Grant no. EIF-BGM-4-RFTF-1/2017-21/04/1-M-02) are acknowledged. We also acknowledge the support by the Basque Departamento de Educacion, UPV/EHU (Grant no. IT-756-13), Spanish Ministerio de Ciencia e Innovación (Grant no. PID2019-103910GB-I00), the Fundamental Research Program of the State Academies of Sciences (line of research III.23.2.9) and Tomsk State University competitiveness improvement program (project no. 8.1.01.2018). I.P.R. acknowledge support from Ministry of Education and Science of the Russian Federation (State Task No. 0721-2020-0033) (tight-binding calculations). The calculations were performed in Donostia International Physics Center and in the Research park of St. Petersburg State University Computing Center (http://cc.spbu.ru).

AUTHOR CONTRIBUTIONS

I.I.K. and M.M.O. have written the manuscript and contributed as co-first authors. The ARPES measurements were carried out by I.I.K., A.M.S., D.E., V.V., S.O.F., A.G.R., G.D.S., L.P., A. Kimura. The SQUID magnetometry has been done by A. Koroleva. and E. S. The samples have been grown and characterized by Z.S.A., M.B.B., I.R.A., O.E.T., and K.A.K. The transport measurements have been carried out by N.M., N.A.A., and V.N.Z. The band structure calculations were performed by M.M.O., M.B.-R., S.V.E., and E.V.C. The exchange coupling constants calculations were performed by M.B.-R., M.M.O., and A.E. Tight-binding calculations were performed by I.P.R. The magnetic anisotropy studies were performed by M.M.O. The Monte Carlo simulations were performed by M.H. The supervision of the project was executed by E.V.C.

COMPETING INTERESTS

The authors declare no competing interests.

ADDITIONAL INFORMATION

Supplementary information is available for this paper at https://doi.org/10.1038/s41535-020-00255-9.

Correspondence and requests for materials should be addressed to I.I.K., M.M.O. or E.V.C.

Reprints and permission information is available at http://www.nature.com/reprints

Publisher's note Springer Nature remains neutral with regard to jurisdictional claims in published maps and institutional affiliations.